Hydrodynamics and Brownian motions of a spheroid near a rigid wall

M. De Corato, F. Greco, G. D'Avino, and P. L. Maffettone

Citation: The Journal of Chemical Physics **142**, 194901 (2015); doi: 10.1063/1.4920981
View online: http://dx.doi.org/10.1063/1.4920981
View Table of Contents: http://scitation.aip.org/content/aip/journal/jcp/142/19?ver=pdfcov
Published by the AIP Publishing

Hydrodynamics and Brownian motions of a spheroid near a rigid wall

M. De Corato,[1,a)] F. Greco,[2] G. D'Avino,[1] and P. L. Maffettone[1]
[1]*Dipartimento di Ingegneria Chimica, dei Materiali e della Produzione Industriale, Universitá di Napoli Federico II, P.le Tecchio 80, 80125 Naples, Italy*
[2]*Istituto di Ricerche sulla Combustione, IRC-CNR, P.le Tecchio 80, 80125 Naples, Italy*

(Received 21 January 2015; accepted 30 April 2015; published online 15 May 2015)

In this work, we study in detail the hydrodynamics and the Brownian motions of a spheroidal particle suspended in a Newtonian fluid near a flat rigid wall. We employ 3D Finite Element Method (FEM) simulations to compute how the mobility tensor of the spheroid varies with both the particle-wall separation distance and the particle orientation. We then study the Brownian motion of the spheroid by means of a discretized Langevin equation. We specifically focus on the additional drift terms arising from the position and orientational dependence of the mobility matrix. In this respect, we also propose a numerically convenient approximation of the orientational divergence of the mobility matrix that is required in the solution of the Langevin equation. Our results illustrate that both hydrodynamics and Brownian motions of a spheroidal particle near a confining wall display novel features from those of a sphere in the same type of confinement. © *2015 AIP Publishing LLC.* [http://dx.doi.org/10.1063/1.4920981]

I. INTRODUCTION

The characterization of the dynamics of colloidal particles suspended in fluids in confined geometries is of interest in several fields such as microfluidics,[1] medicine,[2] and interface analysis.[3] It is well-known that the diffusive behavior of particles in the presence of confining walls is dramatically different from that occurring in the bulk, due to the arising of hydrodynamic interactions between the particle and the walls.[4,5]

The diffusion of a sphere in confined geometries has been extensively studied through experiments. Several geometries have been considered, such as a single planar wall,[6–9] two parallel walls,[10–12] and a cylindrical cavity.[13] The results clearly show that the dependence of the translational diffusion coefficients on particle position reflects the hydrodynamic interactions that the particle experiences under confinement, for which theoretical predictions are well established.[4] In other words, a generalized Stokes-Einstein relationship holds, linking the local diffusivity to a space-dependent friction matrix or, equivalently, a space-dependent mobility matrix, to be evaluated for the specific geometry at hand.

In the case of non-spherical particles, also the rotational diffusivity needs to be evaluated, and roto-translational couplings may become important, especially in confined geometries.[14] On the experimental side, even for the simplest case of axisymmetric particles (e.g., rods or spheroids), tracking of the orientation of the axis of symmetry is required, which is, of course, much more difficult than tracking of the center of mass. For this reason, the first experimental measurements have been limited to particles strongly confined between two parallel walls[15–18] (quasi-2D confinement), where the particle axis of symmetry remains around the gap midplane, parallel to the walls. Quite recently, the 3D tracking of both orientation and center of mass of elongated particles has been reported.[19–21] Measurements of the rotational diffusivities of nanorods tethered to a rigid wall confirm that the diffusion process is well predicted through hydrodynamic simulations giving the friction matrix.[22]

Many examples of numerical simulations on Brownian non-spherical particles are reported in the recent literature. Brownian dynamics simulations of unbounded suspensions of rod-like particles[23–27] and arbitrarily shaped particles[28–30] have been carried out for different volume fractions, ranging from dilute to concentrated regimes, although interparticle hydrodynamic interactions are often neglected. The inclusion of hydrodynamic interactions gives rise to "corrective terms" in the Brownian dynamics.[31,32] In this regard, Padding and Briels[33] recently computed the friction of a rod immersed in a Newtonian liquid near a single planar wall. A stochastic rotation dynamics method was employed,[34] and a shish-kebab model was used to describe the rodlike particle. The translational and rotational friction tensors were calculated for different orientations and particle-wall distances. Due to computational limitations, however, a relatively small simulation box was used that, according to the authors themselves,[33] induces some spurious self-interaction with periodic images of the rod and hydrodynamic interactions with the second (far) wall.

In this paper, we present a detailed study on (i) the hydrodynamic interactions and (ii) the resulting hindered Brownian motion of a spheroidal particle suspended in a quiescent Newtonian fluid in the proximity of a rigid flat wall. In the first part of the paper, the translational, rotational, and roto-translational mobility matrices are computed by finite element simulations in the whole range of possible orientations and particle-wall distances, from an almost touching particle to very large distances from the wall, so that the unbounded conditions are recovered. In the second part of the paper, we exploit the computed mobility matrices to investigate the

a)marco.decorato@unina.it

effects of the spheroid-wall hydrodynamic interactions on the Brownian motion. A Langevin equation, properly modified to account for space-dependent mobility coefficients, is considered and numerically solved. Results on the translational and rotational drifts induced by the confining wall are presented.

The paper is organized as follows: in Sec. II, the hydrodynamic problem of a rigid body in Stokes regime is briefly reviewed; the spheroid-wall geometry and the relevant hydrodynamic governing equations are then presented in Sec. III; in Sec. IV, the mobility matrices computed from finite element numerical simulations are reported; in Sec. V, the discretized version of the Langevin equation and the above-mentioned corrective terms arising from particle-wall hydrodynamic interactions are illustrated; the translational and rotational drift velocities induced by the corrective terms in the Langevin equation are presented in Sec. VI; finally, some conclusions are drawn in Sec. VII.

II. RIGID BODY STOKES HYDRODYNAMICS

In this section, we briefly recall how the dynamics of an arbitrary rigid body suspended in a Newtonian fluid at vanishing Reynolds numbers (Stokes limit) is formulated. Linearity of Stokes hydrodynamics implies that the equations of motion of the rigid body can be represented by a linear system relating the particle translational velocity $\boldsymbol{u}$ and rotational velocity $\boldsymbol{\omega}$ to the force $\boldsymbol{F}$ and torque $\boldsymbol{T}$ that are externally applied to the particle (resistance problem),[4]

$$\begin{pmatrix} \boldsymbol{F} \\ \boldsymbol{T} \end{pmatrix} = \mathbf{Z} \cdot \begin{pmatrix} \boldsymbol{u} \\ \boldsymbol{\omega} \end{pmatrix}. \tag{1}$$

In this equation, the matrix $\mathbf{Z}$ is the so-called "friction" or "resistance" matrix. Such a matrix can be further decomposed as

$$\mathbf{Z} = \begin{bmatrix} \mathbf{Z}_a & \mathbf{Z}_b \\ \mathbf{Z}_b^T & \mathbf{Z}_c \end{bmatrix}. \tag{2}$$

It can be shown[4] that the friction matrix is symmetric and positive definite. From the symmetry property, it follows that the sub-matrices $\mathbf{Z}_a$ and $\mathbf{Z}_c$ are symmetric as well. By using the definitions in Eq. (2), Eq. (1) can be equivalently written in expanded form as

$$\begin{cases} \boldsymbol{F} = \mathbf{Z}_a \cdot \boldsymbol{u} + \mathbf{Z}_b \cdot \boldsymbol{\omega} \\ \boldsymbol{T} = \mathbf{Z}_b^T \cdot \boldsymbol{u} + \mathbf{Z}_c \cdot \boldsymbol{\omega} \end{cases}. \tag{3}$$

Of course, one may choose to consider the "inverse problem" as well (mobility problem), where the unknowns $\boldsymbol{u}$ and $\boldsymbol{\omega}$ are given by

$$\begin{pmatrix} \boldsymbol{u} \\ \boldsymbol{\omega} \end{pmatrix} = \mathbf{M} \cdot \begin{pmatrix} \boldsymbol{F} \\ \boldsymbol{T} \end{pmatrix}. \tag{4}$$

The symmetric and positive definite matrix $\mathbf{M}$ is the so-called "mobility matrix," which can be itself partitioned as

$$\boldsymbol{M} = \begin{bmatrix} \boldsymbol{M}_a & \boldsymbol{M}_b \\ \boldsymbol{M}_b^T & \boldsymbol{M}_c \end{bmatrix}, \tag{5}$$

with analogous symmetry properties as those of the friction matrix, i.e., with both the submatrices $\boldsymbol{M}_a$ and $\boldsymbol{M}_c$ being symmetric. Equation (4) can then be written as

$$\begin{cases} \boldsymbol{u} = \boldsymbol{M}_a \cdot \boldsymbol{F} + \mathbf{M}_b \cdot \boldsymbol{T} \\ \boldsymbol{\omega} = \boldsymbol{M}_b^T \cdot \boldsymbol{F} + \boldsymbol{M}_c \cdot \boldsymbol{T} \end{cases}. \tag{6}$$

Of course, from Eqs. (1) and (4), the mobility and the friction matrices are related by an inversion relation $\boldsymbol{M} = \boldsymbol{Z}^{-1}$. The friction and mobility matrices contain all the information about the rigid body shape and about the hydrodynamic interactions between the particle and the boundaries, if any.

III. GOVERNING EQUATIONS

We address now the hydrodynamic problem of a freely buoyant rigid spheroid suspended in an incompressible Newtonian liquid in proximity of a rigid flat wall. The problem of an axisymmetric particle near a boundary has been partially investigated in previous works;[35,36] the method used in those papers (boundary integral method) is different from that used in the present work (see below). Moreover, we compute the complete mobility matrices, whereas only specific configurations were considered in the references indicated above. We first present the geometry and the adopted coordinate system; then, we discuss the governing equations and the procedure used to solve them, and thereafter compute the mobility matrix $\boldsymbol{M}$ from Eq. (6) above.

As depicted in Fig. 1(a), a Cartesian reference frame with the origin on the wall and the z-axis normal to the wall is considered. The particle center of volume $\boldsymbol{r}$ is located on the z-axis. Furthermore, without loss of generality, we select the x-axis of the reference frame coinciding with the projection along z of the spheroid major axis on the wall. We denote with a the length of the major semi-axis and with b the length of the minor semi-axis. The particle *aspect ratio* is then defined as $AR = a/b$. The distance between the particle center of volume and the wall is denoted by h, and the angle between the major axis and the wall normal vector $\boldsymbol{n}$ is denoted with θ, so that $\theta = \pi/2$ identifies a spheroid parallel to the wall.

Due to the geometry considered in this work, i.e., that of a spheroid in proximity of a single infinite flat wall, for any given particle-wall distance h, all configurations obtained by rotating the spheroid around the z-axis, i.e., for the same values of the angle θ, are equivalent. Consequently, the particle-wall hydrodynamic interactions and, in turn, the friction and mobility matrices are functions of h and θ only, i.e., $\mathbf{Z} = \mathbf{Z}(h,\theta)$ and $\boldsymbol{M} = \boldsymbol{M}(h,\theta)$. Because of the invariance for rotations around z, it is sufficient to compute the mobility (or friction) matrix only for configurations with the major axis of the spheroid lying in the xz-plane; the mobility or friction matrices for orientations outside the xz-plane are simply obtained by rotations around z.

In this work, we compute the friction matrix by first solving the Stokes equations,

$$\begin{cases} \boldsymbol{\nabla} \cdot \boldsymbol{v} = 0 \\ -\boldsymbol{\nabla} p + \mu \nabla^2 \boldsymbol{v} = 0 \end{cases} \tag{7}$$

that governs the fluid dynamics of an incompressible Newtonian fluid under the assumption of inertialess conditions. In

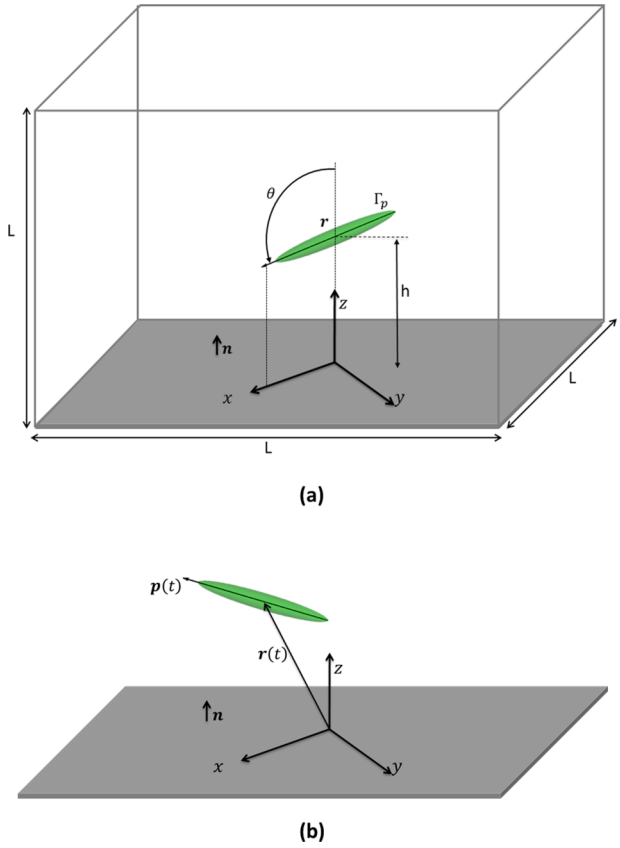

FIG. 1. (a) Schematic representation of a spheroid near a flat planar wall and of the coordinate system employed. The cubic computational box of side L is also shown. (b) Representation of the orientation vector $\boldsymbol{p}$ and the center of mass vector $\boldsymbol{r}$.

these equations, $\boldsymbol{v}$, p, and μ are the velocity, pressure, and viscosity of the fluid, respectively. The following boundary conditions apply:

$$\begin{cases} \boldsymbol{v} = \boldsymbol{u} + \boldsymbol{\omega} \times (\boldsymbol{r}_s - \boldsymbol{r}) & \text{on } \Gamma_p \\ \boldsymbol{v} = 0 & \text{on } \Gamma_w \end{cases}, \tag{8}$$

where $\boldsymbol{r}_s - \boldsymbol{r}$ denotes the distance vector of a point $\boldsymbol{r}_s$ on the spheroid surface from the spheroid center of volume $\boldsymbol{r}$, and the surfaces Γ_p and Γ_w are the particle surface and the boundaries of the cubic computational box, as depicted in Fig. 1(a). Both equations in Eq. (8) express "no-slip conditions." The first equation accounts for the rigid-body motion of the particle, whereas the second equation expresses the quiescent conditions of the fluid "far" from the particle, i.e., at the physical wall $z = 0$, and at the other (virtual) walls of the computational box.

By imposing the particle translational and rotational velocities $\boldsymbol{u}$ and $\boldsymbol{\omega}$, respectively, the system of equations is numerically solved by a standard Galerkin-finite element method in the cubic box with length L. A boundary-fitted mesh with tetrahedral elements is used. A quadratic continuous interpolation ($P2$) is used for the velocity and a linear continuous interpolation ($P1$) is used for the pressure. Mesh convergence has been verified for all the calculations presented in this work. A finer mesh is required when the particle is close to the wall in order to accurately solve the fields between the spheroid and the wall. The total number of elements varies between about 60 000 and 120 000. Since the computational box is meant to represent a semi-infinite 3D domain, to guarantee unperturbed conditions far from the particle, the length L is chosen such that $L \gg h$ and $L \gg a$. Preliminary results show that $L = 40a$ is sufficient to neglect the effects of the virtual walls. In fact, we verified that when the particle is located in the middle of our computational domain, the discrepancy between the calculated friction matrix and its available analytical expression for an unconfined spheroid[4] is always less than 3%. Once the pressure and velocity fields corresponding to the given $(\boldsymbol{u}, \boldsymbol{\omega})$ couple are obtained, the drag force and torque acting on the particle are readily computed through

$$\begin{aligned} \boldsymbol{F} &= \int_{\Gamma_p} \left[-p\boldsymbol{I} + \mu(\boldsymbol{\nabla v} + \boldsymbol{\nabla v}^T)\right] \cdot \boldsymbol{n}_p \, d\Gamma_p, \\ \boldsymbol{T} &= \int_{\Gamma_p} (\boldsymbol{r}_s - \boldsymbol{r}) \times \left[(-p\boldsymbol{I} + \mu(\boldsymbol{\nabla v} + \boldsymbol{\nabla v}^T)) \cdot \boldsymbol{n}_p\right] d\Gamma_p, \end{aligned} \tag{9}$$

where $\boldsymbol{n}_p$ is the local normal to the particle surface, pointing to the fluid. With $\boldsymbol{u}$, $\boldsymbol{\omega}$, $\boldsymbol{F}$, and $\boldsymbol{T}$ known, the friction matrix $\boldsymbol{Z}(h,\theta)$ can now be computed from Eq. (1).

In this regard, we would like to mention that $\boldsymbol{Z}(h,\theta)$ is a symmetric 6×6 matrix with, in general, 21 unknowns. The relationship in Eq. (1), on the other hand, only gives 6 scalar equations. The computation of the friction matrix entries is then actually performed through the following procedure. In each simulation, we impose a single non-zero component of the "particle velocity vector" $(\boldsymbol{u},\boldsymbol{\omega})$ (e.g., u_x), solve the system of Eq. (7) together with boundary conditions (8), and compute $\boldsymbol{F}$ and $\boldsymbol{T}$ through Eq. (9). The set of Eq. (1), however, contains now 6 unknowns only (e.g., the first column of the friction matrix, if we imposed u_x) and can then be solved. The procedure is then repeated by imposing the other particle velocity vector components one at a time, i.e., with all the other components being nil. Six iterations then complete the cycle, giving all the entries of the friction matrix. Finally, the mobility matrix is computed by inversion, as it is $\boldsymbol{M}(h,\theta) = \boldsymbol{Z}(h,\theta)^{-1}$.

IV. MOBILITY MATRIX

In this section, we present the mobility matrix resulting from our numerical simulations. All the reported results refer to a spheroidal particle with aspect ratio $AR = 8$, which is sufficiently far from a spherical shape and, hence, strong deviations from the isotropic case are expected. On the other hand, the aspect ratio is well below the value such that a slender-body approximation can be applied. As mentioned above, $\boldsymbol{M}(h,\theta)$ is a 6×6 symmetric matrix with 21 independent components. However, due to the symmetries of the problem, 9 out of such 21 components are in fact zero, as described below.

To efficiently capture the dependence of the mobility matrix $\boldsymbol{M}$ on h and θ, the computations are performed on a predetermined grid of points in the space (h,θ). More specifically, the distance h is varied in the range $[0, 120b]$ that is divided in 120 points. A non-uniform grid is selected, with smaller intervals for lower values of h, i.e., near the wall, where larger gradients of the mobility matrix are expected. The angle θ varies in the range $[0,\pi]$ that is divided in 61 uniformly distributed points. For each grid point, convergence

of the numerical solution of the corresponding hydrodynamic problem is of course checked by running simulations with different mesh sizes.

A further observation concerning the mobility matrix $\boldsymbol{M}(h,\theta)$ is as follows. The mobility coefficients as $h \to \infty$ must of course become those pertaining to an unbounded spheroid. It should be emphasized, however, that this asymptotic behavior does not necessarily imply that these coefficients are independent from θ, because of our choice for the reference frame, in which the x-axis coincides with the projection of the major axis (see Fig. 1(a)). In other words, the mobility coefficients that become independent from the angular position in the unbounded case are those computed along the principal axes of the spheroid, not those of Eqs. (10)–(12) below.

In Subsections IV A–IV C, we present the trends of the coefficients of the sub-matrices $\boldsymbol{M}_a(h,\theta)$, $\boldsymbol{M}_b(h,\theta)$, and $\boldsymbol{M}_c(h,\theta)$ that form the complete mobility matrix $\boldsymbol{M}(h,\theta)$, as reported in Eq. (5). All the quantities are presented in dimensionless form. The distance h is made dimensionless by the spheroid minor axis length $2b$. Therefore, when the spheroid is oriented with its major axis parallel (orthogonal) to the wall, the minimum dimensionless distance (i.e., the particle touches the wall) is $h = 0.5$ ($h = 4$). The components of the matrices $\boldsymbol{M}_a(h,\theta)$, $\boldsymbol{M}_b(h,\theta)$, and $\boldsymbol{M}_c(h,\theta)$ are made dimensionless by multiplication with the fluid viscosity μ times the quantities $(2b)$, $(2b)^2$, and $(2b)^3$, respectively.

A. Translational mobility

The translational mobility matrix $\boldsymbol{M}_a(h,\theta)$ is a symmetric matrix with the following non-zero entries (for the problem investigated here):

$$\boldsymbol{M}_a(h,\theta) = \begin{bmatrix} M_{a,xx}(h,\theta) & 0 & M_{a,xz}(h,\theta) \\ 0 & M_{a,yy}(h,\theta) & 0 \\ M_{a,xz}(h,\theta) & 0 & M_{a,zz}(h,\theta) \end{bmatrix}. \quad (10)$$

Indeed, since $y = 0$ is a plane of symmetry, no coupling between a force in the y-direction and a velocity in the other two directions can exist, implying that $M_{a,xy} = M_{a,zy} = 0$.

In Figs. 2–4, we report the coefficients $M_{a,xx}(h,\theta)$, $M_{a,yy}(h,\theta)$, and $M_{a,zz}(h,\theta)$, respectively. In these figures, we only report the interval $\theta \in [0,\pi/2]$, because the three coefficients are symmetric around $\theta = \pi/2$ (and of course around $\theta = 0$). For any given h, the qualitative behavior of the mobility coefficients is essentially unchanged from that of an unbounded spheroid ($h \to \infty$). Notice however that, for a fixed θ, all the mobility coefficients show a monotonic reduction as the spheroid approaches the wall, with an abrupt fall to zero in close proximity of the wall. From Figs. 2–4, the coefficient $M_{a,zz}(h,\theta)$ is seen to be the most rapidly changing one when varying (h,θ), meaning that the motion in direction normal to the wall is the most affected by hydrodynamic interactions.

In Fig. 5, we show the calculated "mixed" coefficient $M_{a,xz}(h,\theta)$ that represents the translational coupling of directions x (velocity) and z (force). We only report the interval $\theta \in [0,\pi/2]$: indeed, $M_{a,xz}(h,\theta)$ is antisymmetric around

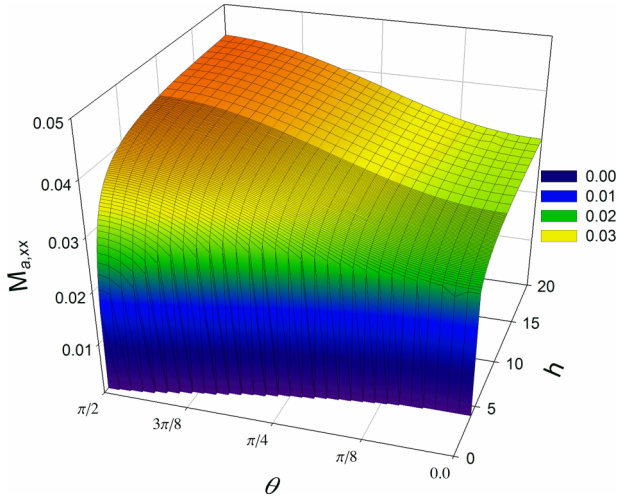

FIG. 2. Dimensionless mobility coefficient $M_{a,xx}$ as a function of h and θ. The steep vertical lines and the sudden decrease of $M_{a,xx}$ from a finite value to 0 mean that the spheroid approaches an excluded volume configuration. Note that $M_{a,xx}$ is symmetric with respect to $\theta = 0$ and $\theta = \pi/2$.

$\theta = 0$ and $\theta = \pi/2$. At variance with the other components of the translational mobility matrix, the coefficient $M_{a,xz}(h,\theta)$ shows a maximum in the interval $\theta \in [0,\pi/2]$, at $\theta \sim \pi/4$ (and a corresponding minimum in $\theta \in [\pi/2,\pi]$). We again remark that the trend of $M_{a,xz}(h,\theta)$ for large h-values results from the choice of the reference frame as in Fig. 1(a). Indeed, it can be shown that, as h becomes infinity, $M_{a,xz}$ is proportional to the mobilities along the principal axes of the spheroid through the factor $\sin(\theta)\cos(\theta)$, which is exactly the large-h results of our simulations. As the spheroid approaches the wall, it can be seen that the reduction of $M_{a,xz}(h,\theta)$ induced by the presence of the wall is quite modest, except for extremely small particle-wall distances.

B. Rotational mobility

The rotational mobility matrix $\boldsymbol{M}_c(h,\theta)$ is a symmetric matrix and, on the basis of the same symmetry arguments used

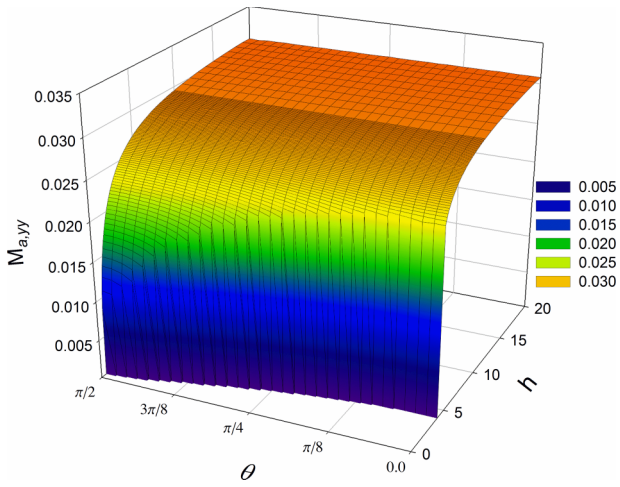

FIG. 3. Dimensionless mobility component $M_{a,yy}$ as a function of h and θ. Note that $M_{a,yy}$ is symmetric with respect to $\theta = 0$ and $\theta = \pi/2$.

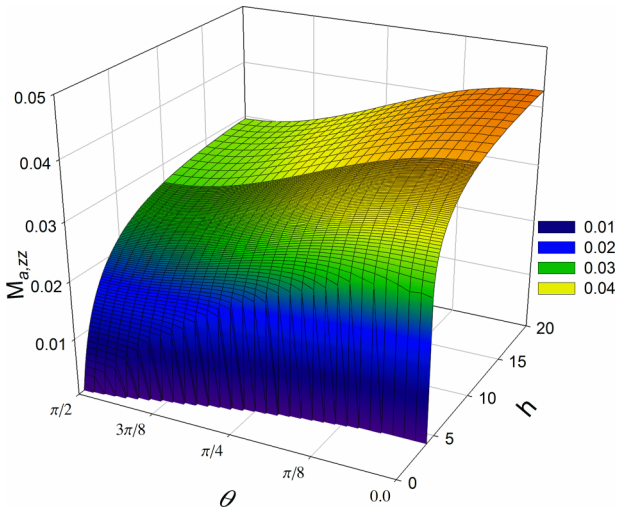

FIG. 4. Dimensionless mobility component $M_{a,zz}$ as a function of h and θ. Note that $M_{a,zz}$ is symmetric with respect to $\theta = 0$ and $\theta = \pi/2$.

for the matrix $\boldsymbol{M}_a(h,\theta)$, it has to be in the form

$$\boldsymbol{M}_c(h,\theta) = \begin{bmatrix} M_{c,xx}(h,\theta) & 0 & M_{c,xz}(h,\theta) \\ 0 & M_{c,yy}(h,\theta) & 0 \\ M_{c,xz}(h,\theta) & 0 & M_{c,zz}(h,\theta) \end{bmatrix}, \quad (11)$$

i.e., it contains only four distinct nonzero coefficients. In Figs. 6 and 7, we report the coefficients $M_{c,xx}(h,\theta)$ and $M_{c,yy}(h,\theta)$. (For the sake of brevity, we choose to not report the plot of $M_{c,zz}(h,\theta)$, as the behavior of this component is qualitatively similar to that of $M_{c,xx}(h,\theta)$.) In these figures, we only report the interval $\theta \in [0,\pi/2]$ (the two coefficients are symmetric around $\theta = \pi/2$, and of course around $\theta = 0$). Figures 6 and 7 clearly show that the diagonal rotational mobilities are only marginally reduced as h becomes smaller, remaining in fact constant up to distances that are lower than the ellipsoid major semi-axis. For what matters the $M_{c,yy}(h,\theta)$ coefficient, the angle θ has a small influence as well. The $M_{c,xx}(h,\theta)$ coefficient, instead, is much more affected by θ variations. This can be explained by noticing that when θ is equal to $\pi/2$,

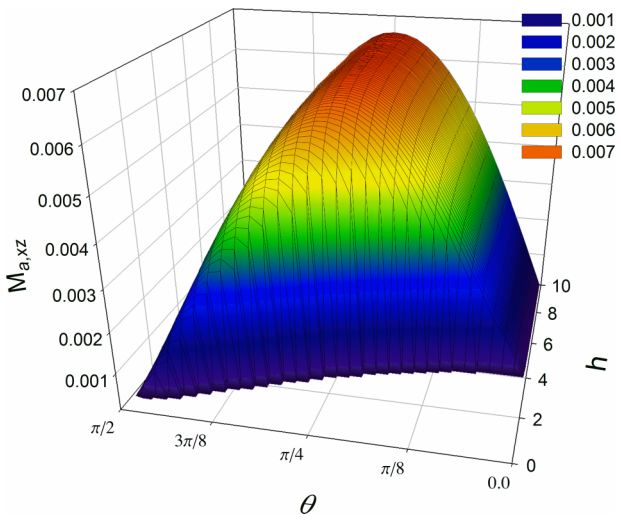

FIG. 5. Dimensionless mobility component $M_{a,xz}$ as a function of h and θ. Note that $M_{a,xz}$ is anti-symmetric with respect to $\theta = 0$ and $\theta = \pi/2$.

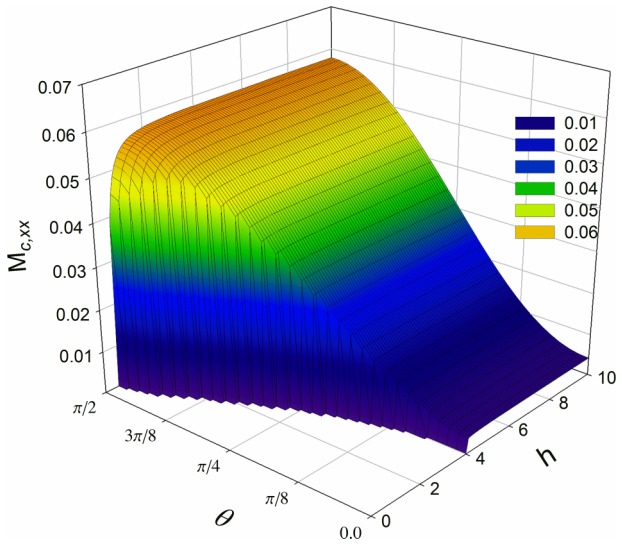

FIG. 6. Dimensionless mobility component $M_{c,xx}$ as a function of h and θ. Note that $M_{c,xx}$ is symmetric with respect to $\theta = 0$ and $\theta = \pi/2$.

$M_{c,xx}(h,\theta)$ represent the "spin" rotational mobility, i.e., the mobility pertaining to a rotation around the spheroid major axis. Such a mobility is of course larger than the xx rotational mobility when the spheroid is almost perpendicular to the wall ($\theta \approx 0$), i.e., for rotations (almost) around the spheroid minor axis. Notice that also in this case (similarly to what said for the translational mobilities), the dependence on θ of the mobility coefficient $M_{c,xx}(h,\theta)$ as h goes to infinity is related to the choice of the fixed reference frame.

Finally, the rotational mixed component $M_{c,xz}(h,\theta)$ has a behavior qualitatively similar to the translational coefficient $M_{a,xz}(h,\theta)$ (see Fig. 5). For brevity then, we choose to not report the corresponding plot.

C. Rotation-translation coupling mobility

The rotation-translation coupling mobility matrices $\boldsymbol{M}_b(h,\theta)$ or $\boldsymbol{M}_b^T(h,\theta)$, as noted in Eq. (6), relate the translational velocity to an applied torque and the rotational velocity

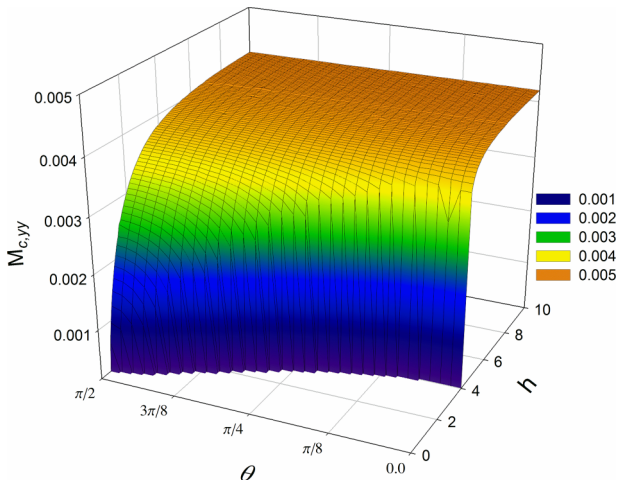

FIG. 7. Dimensionless mobility component $M_{c,yy}$ as a function of h and θ. Note that $M_{c,yy}$ is symmetric with respect to $\theta = 0$ and $\theta = \pi/2$.

to an applied force, respectively. Since it seems to us easier to understand the roto-translational coupling effects by considering the resulting rotational velocity when a force is applied to the center of volume of the spheroid, we choose to discuss here the $\boldsymbol{M}_b^T(h,\theta)$ only.

The sub-matrix $\boldsymbol{M}_b^T(h,\theta)$ is, in general, a non-symmetric matrix.[4,28] The situation considered in this work, however, implies that $\boldsymbol{M}_b^T(h,\theta)$ only contains 4 non-zero entries,

$$\boldsymbol{M}_b^T(h,\theta) = \begin{bmatrix} 0 & M^T_{b,xy}(h,\theta) & 0 \\ M^T_{b,yx}(h,\theta) & 0 & M^T_{b,yz}(h,\theta) \\ 0 & M^T_{b,zy}(h,\theta) & 0 \end{bmatrix}. \quad (12)$$

Indeed, since $y = 0$ is a plane of symmetry, a force applied in x- or z-direction cannot induce an angular velocity around the x- or z-axis: hence, components xx, xz, zx, and zz of $\boldsymbol{M}_b^T(h,\theta)$ are nil. In addition, the symmetry of the particle shape with respect to the xz-plane implies that a force along the y-direction cannot induce any angular velocity around y: it is $M^T_{b,yy}(h,\theta) = 0$.

In Fig. 8, we report the coefficient $M^T_{b,yx}(h,\theta)$. (For clarity, we choose to present all the results in this subsection as contour plots.) For a fixed value of h, $M^T_{b,yx}(h,\theta)$ switches from negative values when θ is near $\pi/2$ (spheroid almost parallel to the wall) to positive values when θ approaches either 0 or π. The solid curve in the figure is the set of (h,θ) couples where $M^T_{b,yx}(h,\theta) = 0$; within the tongue-like region delimited by such a curve, the coefficient is negative, outside it is positive. A negative/positive value of $M_{b,xy}(h,\theta)$ means that the spheroid, dragged along positive x, will rotate so that its "leading edge" (the tip of the spheroid at positive x) moves away from/towards the wall, thus rotating towards smaller/higher values of θ. In other words, for (h,θ) inside the tongue-line region, the spheroid rotates towards the z-direction.

The points on the boundary of the tongue-like region, corresponding to $M^T_{b,yx}(h,\theta) = 0$, are "equilibrium" points, i.e., a force applied to the x-direction does not produce any rotation. Specifically, the lower portion of the curve $M^T_{b,yx}(h,\theta) = 0$ is made of stable equilibrium points θ_{eq}, whereas the upper portion of the curve is made of unstable equilibrium points θ_{eq}^{unst}. Consequently, for whatever value of h, a spheroid dragged in positive x-direction tends to the stable equilibrium orientation $\theta_{\rm eq}$ (pertaining to the given h) if it is $\theta_0 < \theta_{eq}^{unst}$, with θ_0 the initial orientation of the spheroid. All of this is pictorially illustrated by the cartoons in Fig. 8.

Finally, from Fig. 8, we see that, for values of θ close to $\pi/2$, $M^T_{b,yx}(h,\theta)$ has a minimum as the particle is very close to the wall, as shown by the presence of a closed iso-$M_{b,yx}$ curve (the dashed curve in the figure). Externally to such closed curve, $M^T_{b,yx}(h,\theta)$ becomes a monotonic function of h. Precisely, it is a monotonically increasing function inside the tongue-like region and a monotonically increasing function of h outside.

In Fig. 9, we report $M^T_{b,xy}(h,\theta)$. This coefficient rules the rotational velocity in x direction when a force is applied along y. The coefficient is calculated to be always negative. Hence, the rotational velocity along x has the effect of moving the major axis of the spheroid outside the xz-plane, with the "leading edge" moving to positive y values if $\theta_0 \in [0, \frac{\pi}{2}]$ and to negative y values when $\theta_0 \in [\frac{\pi}{2}, \pi]$. The former situation is portrayed in the cartoon of Fig. 9. In the peculiar case ($\theta = \pi/2$), i.e., when the spheroid lies parallel to the wall, there is a residual rotational velocity along the x-axis: the particle is experiencing a small "spin" velocity around its major axis. Such an effect disappears, as it must be, moving away from the wall.

In Fig. 10, the trends of the coefficient $M^T_{b,yz}(h,\theta)$ are reported. For a fixed h, $M^T_{b,yz}(h,\theta)$ is an odd function of θ (around $\frac{\pi}{2}$). A negative value of $M^T_{b,yz}(h,\theta)$ ($\theta \in [0, \frac{\pi}{2}]$) means that a spheroid dragged in the positive z-direction, i.e., going away from the wall, rotates in the xz plane so that the "leading edge" turns away from the wall; the opposite rotation occurs, with the "leading edge" going towards the wall, with positive

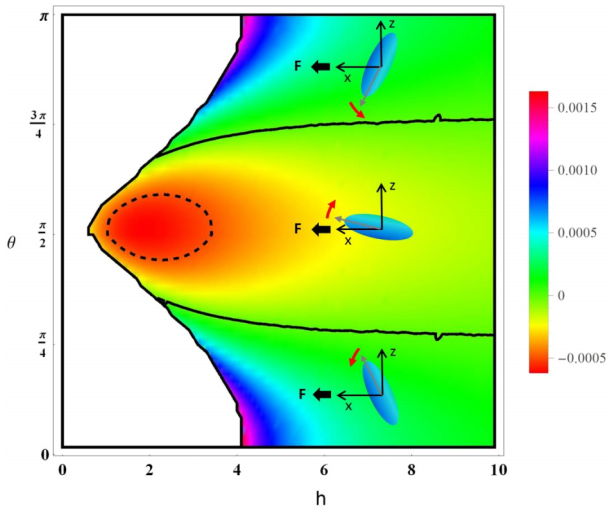

FIG. 8. Dimensionless mobility component $M^T_{b,yx}$ as a function of h and θ. The solid curve on the left separates accessible configurations from excluded volume ones. In the "tongue-like" region, $M^T_{b,yx}$ is negative, and outside it is positive. Thus, roto-translational coupling (force along x and rotation around y) is clockwise in the inner region and counterclockwise outside (see text).

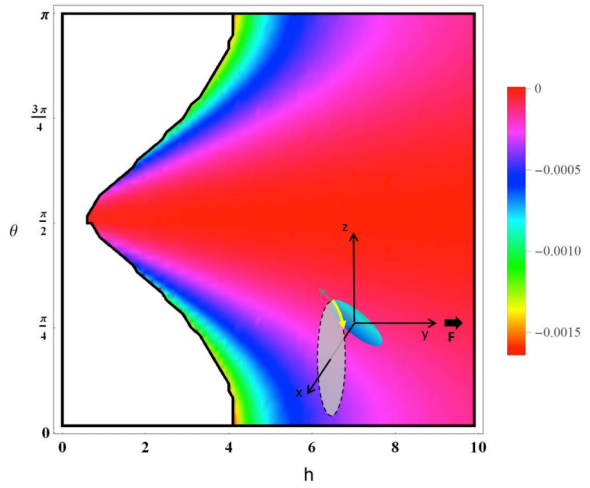

FIG. 9. Dimensionless mobility component $M^T_{b,xy}$ as a function of h and θ. The solid curve on the left separates accessible configurations from excluded volume ones. Notice that $M^T_{b,xy}$ is always negative. Thus, roto-translational coupling (force along y and rotation around x) is always clockwise: the leading tip of the spheroid moves on the circular base of a cone around the x-axis, towards positive y if $\theta < \pi/2$ (see text).

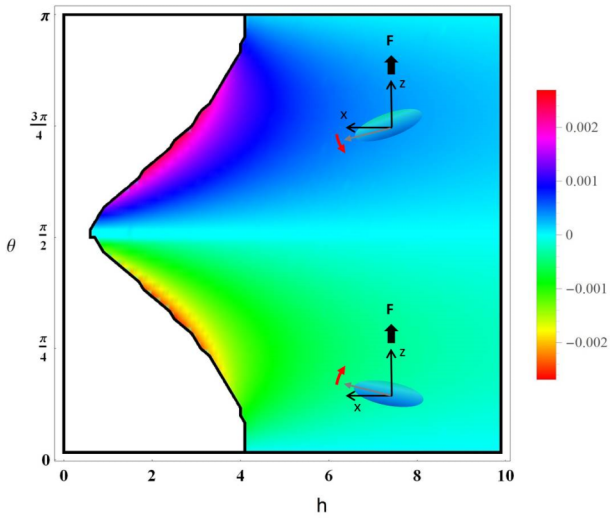

FIG. 10. Dimensionless mobility component $M^T_{b,yz}$ as a function of h and θ. The solid curve on the left separates accessible configurations from excluded volume ones. Because of the change of sign in $M^T_{b,yz}$ with increasing θ, the roto-translational coupling (force along z and rotation around y) is clockwise below $\theta = \pi/2$ and counterclockwise above (see text).

values of $M^T_{b,yz}(h,\theta)$ ($\theta \in [\frac{\pi}{2},\pi]$). In other words, the $\theta = \pi/2$ angular position is an unstable equilibrium point, whereas $\theta = 0$ and $\theta = \pi$ are stable. This is pictorially illustrated by the cartoons in Fig. 10. A spheroid dragged away from a wall will align in the direction normal to the wall itself. We would like to stress that the just described situation is reversed when the dragging force is directed towards the wall, i.e., towards negative z. Indeed, in the latter case, the angular position $\theta = \pi/2$ becomes the stable one: a spheroid dragged towards the wall will become parallel to the wall itself.

In Fig. 11, we plot the trends of $M^T_{b,zy}(h,\theta)$. This coefficient rules the rotational velocity around the z-direction when a force is applied along y. The rotational velocity along z does

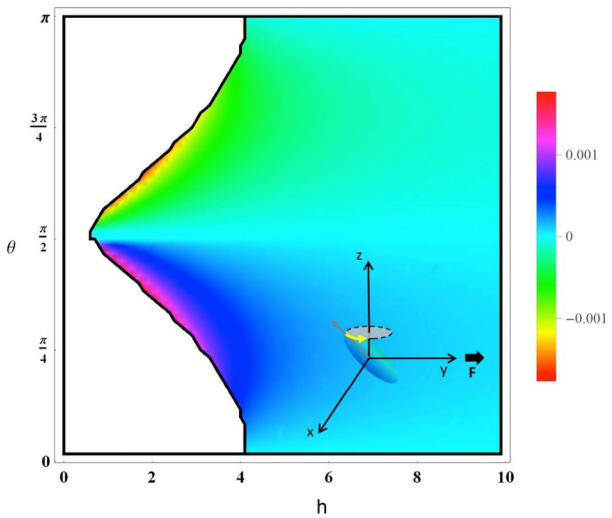

FIG. 11. Dimensionless mobility component $M^T_{b,zy}$ as a function of h and θ. The solid curve on the left separates accessible configurations from excluded volume ones. Because of the change of sign in $M^T_{b,zy}$ with increasing θ, the roto-translational coupling (force along y and rotation around z) is counterclockwise below $\theta = \pi/2$ and clockwise above (see text).

not induce any change in the angle θ, but brings the major axis of the spheroid outside the xz-plane. The coefficient is calculated to be positive in $[0,\frac{\pi}{2}]$ and negative in $[\frac{\pi}{2},\pi]$. Hence, the "leading edge" moves to positive y values if $\theta_0 \in [0,\frac{\pi}{2}]$ (see the cartoon in Fig. 11) and to negative y values when $\theta_0 \in [\frac{\pi}{2},\pi]$. In the peculiar case ($\theta = \pi/2$), i.e., when the spheroid lies parallel to the wall, it remains in the xz-plane.

As a final remark, Figs. 8-11 show that as the spheroid-wall distance h increases, all the components of $\boldsymbol{M}_b(h,\theta)$ vanish: no rotation-translation coupling does exist for an unbounded spheroid. We also point out that the values reported in these figures are one order of magnitude smaller than the components of $\boldsymbol{M}_a(h,\theta)$. However, as it will be discussed later, the sub-matrix $\boldsymbol{M}_b(h,\theta)$ needs to be retained in Brownian dynamics simulations to get the correct spheroid dynamics.

V. SPHEROID BROWNIAN MOTIONS

In Secs. II–IV, a full characterization of the hydrodynamic interactions of a spheroidal particle with a rigid wall has been given. In what follows, we consider the effects of such particle-wall interactions on a spheroidal particle undergoing Brownian motion.

In the literature, the Brownian motion of a rigid particle is typically investigated by two different approaches.[31] One of them is through a generalized diffusion equation, which describes the evolution of a probability distribution function in the degrees of freedom of the particle. Another approach is through a Langevin equation, which directly describes the evolution of the particle's degrees of freedom, giving then a stochastic "trajectory." In this paper, we adopt the Langevin description. In Secs. V A–V D, we present the general equations governing the dynamics of a confined Brownian spheroidal particle, as well as the employed numerical method.

A. Langevin equation

The Langevin equation for a free rigid Brownian particle is a Stochastic Differential Equation (SDE)[37,38] with the stochastic (thermal) forcing modeled by a random noise term accounting for particle mobility. The presence of a spatial confinement induces a configurational dependence of the particle mobilities that, in turn, makes the random noise a multiplicative noise.[39] In integrating the SDE, we prefer to avoid the difficulties related to the interpretation of a stochastic integral containing a multiplicative noise.[39,40] We present instead the Langevin equation directly in a discretized form, which is readily solved.[31] The evolution of a trajectory of a uniaxial particle is fully characterized by its center of mass position vector $\boldsymbol{r}(t)$ and the unit orientation vector $\boldsymbol{p}(t)$ that are represented in Fig. 1(b). Notice that the frame of reference in Fig. 1(b) is defined once and for all at time $t = 0$ and is hereafter referred as the "fixed frame." The discretized form of the Langevin equation for a spheroidal particle suspended in a Newtonian quiescent fluid, in the absence of any inertia and of any external force, reads

$$\boldsymbol{r}(t+\Delta t) = \boldsymbol{r}(t) + \Delta\boldsymbol{r}_B(t) + k_B T[\boldsymbol{\nabla}\cdot\boldsymbol{M}_a(t) + \boldsymbol{\mathcal{R}}\cdot\boldsymbol{M}_b(t)]\Delta t, \tag{13}$$

$$\begin{aligned}\boldsymbol{p}(t+\Delta t) &= \boldsymbol{p}(t) + \Delta\boldsymbol{\Theta}_B(t)\times\boldsymbol{p}(t) + \frac{1}{2}\Delta\boldsymbol{\Theta}_B(t)\\ &\cdot\left[\boldsymbol{p}(t)\Delta\boldsymbol{\Theta}_B(t) - \Delta\boldsymbol{\Theta}_B(t)\boldsymbol{p}(t)\right]\\ &+ k_BT\left[\boldsymbol{\nabla}\cdot\boldsymbol{M}_b^T(t) + \mathcal{R}\cdot\boldsymbol{M}_c(t)\right]\Delta t\times\boldsymbol{p}(t),\end{aligned} \tag{14}$$

where Δt is the time step size and k_BT is the product of the Boltzmann constant k_B times the absolute temperature T. Notice that the matrices $\boldsymbol{M}_a$, $\boldsymbol{M}_b$, and $\boldsymbol{M}_c$, being a function of both the position vector $\boldsymbol{r}(t)$ and the orientation vector $\boldsymbol{p}(t)$, depend on time. Since the time discretization reported in Eqs. (13) and (14) is explicit, these matrices are evaluated at time level t.

The terms $\Delta\boldsymbol{r}_B$ and $\Delta\boldsymbol{\Theta}_B$ in Eqs. (13) and (14) are the standard Brownian translational and angular displacements between time t and time $t+\Delta t$, respectively, defined with respect to the fixed frame. These two terms are vectorial random Gaussian variables defined by the following moments:

$$\begin{aligned}\langle\Delta\boldsymbol{r}_B\rangle &= 0,\\ \langle\Delta\boldsymbol{\Theta}_B\rangle &= 0,\\ \langle\Delta\boldsymbol{r}_B\Delta\boldsymbol{r}_B\rangle &= 2\,\Delta t\,k_BT\boldsymbol{M}_a(\boldsymbol{r}(t),\boldsymbol{p}(t)),\\ \langle\Delta\boldsymbol{\Theta}_B\Delta\boldsymbol{\Theta}_B\rangle &= 2\,\Delta t\,k_BT\boldsymbol{M}_c(\boldsymbol{r}(t),\boldsymbol{p}(t)),\\ \langle\Delta\boldsymbol{r}_B\Delta\boldsymbol{\Theta}_B\rangle &= 2\,\Delta t\,k_BT\boldsymbol{M}_b(\boldsymbol{r}(t),\boldsymbol{p}(t)).\end{aligned} \tag{15}$$

These definitions follow from the fluctuation dissipation theorem[31] that relates the thermal fluctuations in the suspending fluid to the particle-fluid viscous dissipation. As clearly shown in Eq. (15), both $\Delta\boldsymbol{r}_B$ and $\Delta\boldsymbol{\Theta}_B$ are terms of order $\Delta t^{1/2}$, as expected for a random Brownian displacement. Notice that, in Eq. (15), the dependence of the mobility matrices on the instantaneous system configuration is explicitly shown, to highlight how the properties of the stochastic forcing $\Delta\boldsymbol{r}_B$ and $\Delta\boldsymbol{\Theta}_B$ can in fact depend on the position and orientation of the particle in space. This is of course just our case, with the presence of a confining wall.

The term "quadratic" in $\Delta\boldsymbol{\Theta}_B$ (and, hence, linear in Δt) in Eq. (14) is needed to preserve the condition $|\boldsymbol{p}| = 1$ up to order Δt, as explained in Refs. 25 and 28. Indeed, it is readily seen that

$$\langle|\boldsymbol{p}(t+\Delta t)|\rangle = 1 + O(\Delta t^2). \tag{16}$$

Some further observations on this "quadratic" term and on its average are given in Appendix B.

The "convective" terms (explicitly of order Δt) in Eqs. (13) and (14) stem from the spatial and orientational dependence of the matrices $\boldsymbol{M}_a$, $\boldsymbol{M}_b$, and $\boldsymbol{M}_c$,[28,31,39] and are needed to assure that the correct Boltzmann equilibrium distribution is recovered at equilibrium[39] (see also Sec. V D). The leftmost convective terms are the standard spatial divergence of $\boldsymbol{M}_a$ and $\boldsymbol{M}_b^T$, respectively; the other two convective terms in Eqs. (13) and (14) contain instead the "divergence on the unit sphere," i.e., a divergence in the $\boldsymbol{p}$-space (with $|\boldsymbol{p}| = 1$), where the operator $\mathcal{R}$ is defined as follows:[31]

$$\mathcal{R} = \boldsymbol{p}\times\frac{\partial}{\partial\boldsymbol{p}}. \tag{17}$$

Of course, for an unconfined spheroid, all those convective terms vanish, and we recover the classical Langevin equation for an axisymmetric particle.

The above equations are valid for any arbitrarily confined uniaxial particle, by considering the appropriate matrices $\boldsymbol{M}_a$, $\boldsymbol{M}_b$, and $\boldsymbol{M}_c$. Although the principles behind Eqs. (13) and (14) are well known in the literature[31] and many authors have numerically tested the drift terms,[27,30,32,39] to the best of our knowledge, this is the first time that a Langevin equation for a confined uniaxial particle is explicitly in this discretized complete form, fully embodying roto-translational coupling.

B. Generation of the Brownian displacements

For the numerical generation of the Brownian forcings $\Delta\boldsymbol{r}_B$ and $\Delta\boldsymbol{\Theta}_B$ between t and $t+\Delta t$, with moments defined by Eq. (15), the following equations are used:

$$\begin{pmatrix}\Delta\boldsymbol{r}_B\\ \Delta\boldsymbol{\Theta}_B\end{pmatrix} = \sqrt{2k_BT\Delta t}\;\boldsymbol{m}(\boldsymbol{r}(t),\boldsymbol{p}(t))\cdot\begin{pmatrix}\Delta\boldsymbol{N}_1\\ \Delta\boldsymbol{N}_2\end{pmatrix}. \tag{18}$$

In Eq. (18), the matrix $\boldsymbol{m}$ is the square root of the matrix $\boldsymbol{M}$, defined as

$$\boldsymbol{M}(\boldsymbol{r}(t),\boldsymbol{p}(t)) = \boldsymbol{m}(\boldsymbol{r}(t),\boldsymbol{p}(t))\cdot\boldsymbol{m}^T(\boldsymbol{r}(t),\boldsymbol{p}(t)). \tag{19}$$

The matrix $\boldsymbol{m}$ is unique since $\boldsymbol{M}$ is symmetric positive definite. The two vectors $\Delta\boldsymbol{N}_1$ and $\Delta\boldsymbol{N}_2$ are vectorial Gaussian random variables identified by the following moments:

$$\begin{aligned}\langle\Delta\boldsymbol{N}_1\rangle &= 0,\\ \langle\Delta\boldsymbol{N}_2\rangle &= 0,\\ \langle\Delta\boldsymbol{N}_1\Delta\boldsymbol{N}_1\rangle &= \boldsymbol{I},\\ \langle\Delta\boldsymbol{N}_2\Delta\boldsymbol{N}_2\rangle &= \boldsymbol{I},\\ \langle\Delta\boldsymbol{N}_1\Delta\boldsymbol{N}_2\rangle &= 0,\end{aligned} \tag{20}$$

where $\boldsymbol{I}$ is the identity matrix. At each time step, the decomposition of the matrix $\boldsymbol{M}$ according to Eq. (19) is required. In our case, $\boldsymbol{M}$ is a 6×6 matrix, and the decomposition procedure is computationally fast.

C. Random finite difference (RFD)

Solving Eqs. (13) and (14) requires the computation of the translational and orientational divergence terms. As discussed in the first part of the present work, we have pre-computed the mobility matrix on a spatial grid (θ,h) for the case of a uniaxial spheroid in the presence of a wall. Here, then, these data could be directly used to compute the divergence terms. Such operation, however, is computationally expensive.[40] In situations of confinement different from the one considered here, also, a precomputed table for the mobility matrix in all possible system configurations is generally not available. To overcome this problem in general terms, we present an extension of the RFD approximation of the spatial divergence, originally introduced in Delong *et al.*,[41] to the divergence on the unit sphere. As shown in Appendix A, for a given matrix $\boldsymbol{A}(\boldsymbol{r},\boldsymbol{p})$, the following relationships hold:

$$\boldsymbol{\nabla}\cdot\boldsymbol{A}(\boldsymbol{r},\boldsymbol{p}) = \lim_{\epsilon\to0}\frac{1}{\epsilon}\left\langle\left(\boldsymbol{A}(\boldsymbol{r}+\epsilon\Delta\boldsymbol{q},\boldsymbol{p})\cdot\Delta\boldsymbol{q} - \boldsymbol{A}(\boldsymbol{r},\boldsymbol{p})\cdot\Delta\boldsymbol{q}\right)\right\rangle, \tag{21}$$

$$\mathcal{R}\cdot\boldsymbol{A}(\boldsymbol{r},\boldsymbol{p}) = \lim_{\epsilon\to0}\frac{1}{\epsilon}\left\langle\left(\boldsymbol{A}(\boldsymbol{r},\boldsymbol{p}+\epsilon\Delta\boldsymbol{q}\times\boldsymbol{p})\cdot\Delta\boldsymbol{q} - \boldsymbol{A}(\boldsymbol{r},\boldsymbol{p})\cdot\Delta\boldsymbol{q}\right)\right\rangle, \tag{22}$$

where $\Delta \boldsymbol{q}$ is a standard Gaussian random variable defined by the moments

$$\begin{aligned} \langle \Delta \boldsymbol{q} \rangle &= 0, \\ \langle \Delta \boldsymbol{q} \Delta \boldsymbol{q} \rangle &= \boldsymbol{I}. \end{aligned} \tag{23}$$

By discretizing Eqs. (21) and (22) for a finite but small ϵ, we obtain, *on average*, an approximation of the translational and orientational divergences of matrix $\boldsymbol{A}$. Notice that the evaluation of the right-hand sides of Eqs. (21) and (22) requires a random "dummy" update of the particle position and orientation, and the computation of matrix $\boldsymbol{A}$ in this new configuration. The advantage of this procedure is that the small discretization parameter ϵ is not related to the time step size Δt of the "main" numerical integration and can then be chosen as small as possible. In our case, with $\boldsymbol{A}$ representing a mobility sub-matrix, the smallness of ϵ will guarantee to avoid excluded volume problems. Of course, some caution is required to reduce the numerical roundoff.

D. Algorithm verification

In Subsections V A and V B, we have presented and discussed the Langevin equations describing the Brownian motions of a uniaxial particle under a generic confinement. In this subsection, we report some results obtained by the direct solution of such stochastic equations and compare them with computations made from the hydrodynamic calculations illustrated in the first part of the paper. In this way, we aim at obtaining a validation of our numerical algorithm.

First of all, let us show how the spheroid spatial distribution under confinement is correctly described by numerical results from Eqs. (13) and (14), whereas it would be wrongly evaluated in the absence of the "convective" terms, i.e., the terms containing the spatial and angular divergences of the mobility matrices. In Figure 12, numerical results showing the equilibrium probability distribution functions of the particle-wall distance h computed from "complete" (panel (a)) and "incomplete" (panel (b)) Eqs. (13) and (14) are reported. To compute the histograms of the equilibrium probability, we simulated a trajectory of 80×10^6 time steps with $\Delta t = 5 \times 10^{-3}$ (in dimensionless units). We restrict the motion of the spheroid in the interval $h \in [5,9]$ by rejecting the time steps such that the spheroid is displaced outside this interval. The interval is chosen such that the particle experiences no excluded volume effect, but the hydrodynamic interactions with the wall are still relevant, as shown by the mobility trends shown in Sec. IV. It is apparent that the correct description of the spheroid distribution, giving a constant value throughout, is only obtained from the "complete" set of Eqs. (13) and (14).

Additionally, we compute (as an example) the xx translational diffusion coefficient $D_{xx}(h,\theta)$ of a spheroid near a rigid wall. Such diffusion coefficient is obtained in two ways, (i) through the Stokes-Einstein equation,

$$D_{xx}(h,\theta) = k_B T M_{a,xx}(h,\theta), \tag{24}$$

with the mobility matrix coefficient calculated directly from hydrodynamics, and (ii) through the spheroid Mean Square Displacement (MSD) along x, pertaining to a given Δt,

$$D_{xx}(h,\theta) = \frac{\langle \Delta r_x^2(h,\theta) \rangle}{2\Delta t} \tag{25}$$

that is computed by solving Eqs. (13) and (14). Of course, in order to solve the stochastic equations, the hydrodynamics calculations are needed as well, to obtain the mobility matrices entering the Brownian displacements and the convective terms in Eqs. (13) and (14).

For any given initial particle-wall distance h and orientation θ, we released 10^6 spheroids and correspondingly solved one time step Δt of Langevin equations (13) and (14); the average in Eq. (25) was then calculated from those results. Of course, it has also been checked that averages calculated with larger time steps always led to the same diffusion coefficient, i.e., that the originally adopted Δt was "small enough." The just described procedure at a given (h,θ) couple was then repeated for a grid with h varying from 1 to 20, and θ uniformly distributed between 0 and $\frac{\pi}{2}$.

In Fig. 13, we report $D_{xx}(h,\theta)$ computed with both Eq. (25) (circles) and Eq. (24) (surface). Agreement between the two computations is extremely good. The same level of agreement is also found for other entries of the diffusivity tensor (not shown). All of this validates the adopted numerical method and opens the way to the calculations of drift effects (ensuing from confinement) through the Langevin approach, to be discussed in Sec. VI.

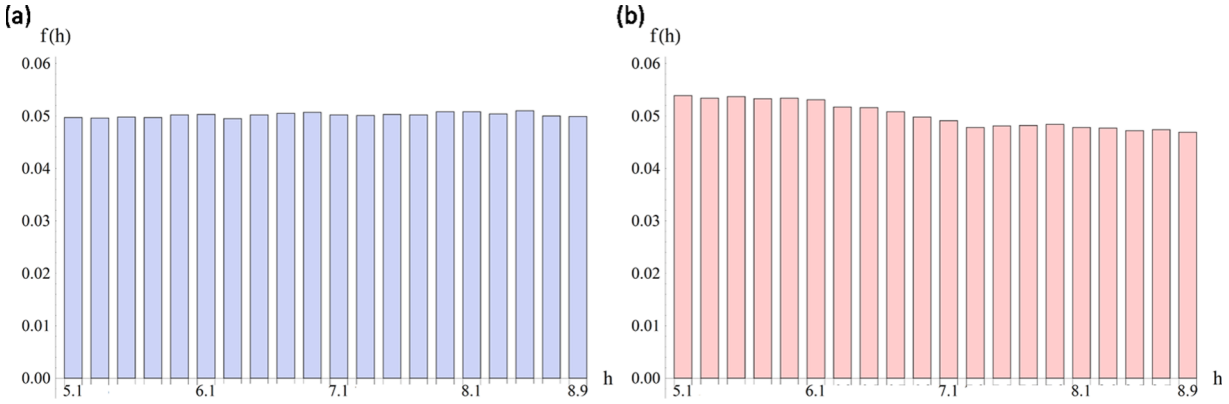

FIG. 12. Equilibrium probability distribution functions of the particle-wall distance h computed through Eqs. (13) and (14) including (a) and not including (b) the spatial and angular divergences of the mobility matrices.

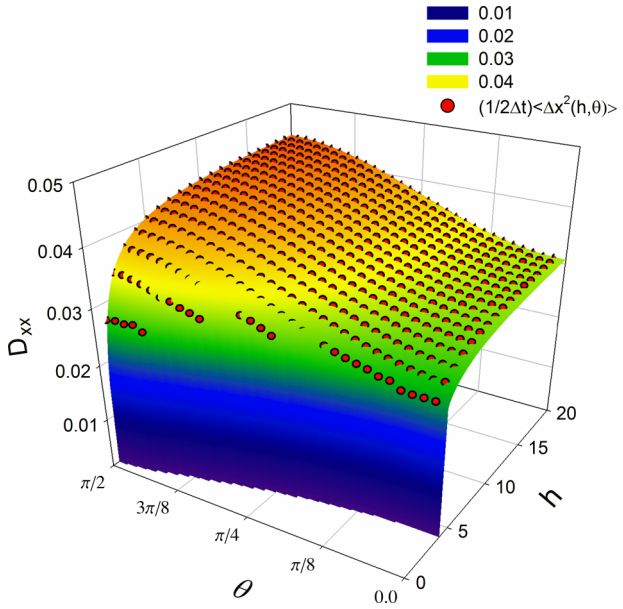

FIG. 13. Comparison between $D_{xx}(h,\theta)$ computed through Eq. (25) (circles, from Brownian dynamics) and Eq. (24) (surface, from hydrodynamics).

VI. SPHEROID DRIFT VELOCITIES

In this section, we investigate the drift effects induced on a Brownian spheroid by particle-wall hydrodynamic interactions. Theoretical results show that a sphere undergoing Brownian motion under confinement (hence, with a space-dependent mobility matrix) experiences a net drift velocity proportional to the divergence of the mobility matrix.[39] Recently, experimental measurements showed the existence of asymmetric Brownian displacements of the sphere center of mass in proximity of a rigid wall.[7] Other experiments measured the drift velocity of spheres in a divergent parallel plate geometry and confirmed the proportionality with the divergence of the mobility matrix.[42] The existence of this drift velocity must be accounted for when measuring the effect of external potentials on the Brownian motion.[43] Indeed, recent experiments showed that neglecting the drift velocity leads to an erroneous qualitative evaluation of the conservative forces acting on Brownian spheres.[44] We would like to point out that the presence of a "drift" velocity does not mean that there is a net particle flux in the velocity direction. The drift velocity is, instead, an effect of the variation of the particle mobility with the configuration of the system, and its adequate evaluation is required to obtain the correct particle equilibrium distribution.

To fully characterize the behavior of a spheroidal particle near a rigid wall, we use the same coordinate system described in Sec. III and shown in Fig. 1(a). In this reference frame, it is sufficient to evaluate the drift velocity at any h-value only for orientations of the spheroid in the xz-plane. Indeed, drift velocities for other orientations (out of the $xz-$ plane) can be readily obtained by a rotation around the z-axis. Hence, the drift velocity is a function of h and θ. At variance with the spherical particle case, we distinguish two drift velocities: a translational drift velocity defined as

$$\left\langle \frac{\Delta \boldsymbol{r}(h,\theta)}{\Delta t} \right\rangle = k_B T[\boldsymbol{\nabla}\cdot\boldsymbol{M}_a(h,\theta) + \boldsymbol{\mathcal{R}}\cdot\boldsymbol{M}_b(h,\theta)] \quad (26)$$

and a rotational drift velocity given by

$$\left\langle \frac{\Delta \boldsymbol{p}(h,\theta)}{\Delta t} \right\rangle = k_B T\left[\boldsymbol{\nabla}\cdot\boldsymbol{M}_b^T(h,\theta) + \boldsymbol{\mathcal{R}}\cdot\boldsymbol{M}_c(h,\theta)\right]\times\boldsymbol{p}(\theta) + \left\langle \frac{1}{2\Delta t}\Delta\boldsymbol{\Theta}_B(t)\cdot[\boldsymbol{p}(t)\Delta\boldsymbol{\Theta}_B(t) - \Delta\boldsymbol{\Theta}_B(t)\boldsymbol{p}(t)]\right\rangle. \quad (27)$$

In Eqs. (26) and (27), the left-hand sides are averages of fluctuating quantities (position and orientation). On the right-hand sides of those equations, the terms containing the spatial and angular divergences are deterministic, whereas the last term of Eq. (27) is still written as an average to be computed: actual averaging is worked out in Appendix B.

It is useful to underline, at this stage, that the translational drift for a spherical particle only contains the term $k_B T\boldsymbol{\nabla}\cdot\boldsymbol{M}_a$. Indeed, even if a sphere might actually experience a nonzero roto-translational coupling, the term $k_B T\boldsymbol{\mathcal{R}}\cdot\boldsymbol{M}_b$ is zero because a sphere has no intrinsic orientation.

The computation of the drift velocities requires the evaluation of the divergence of the various terms of the mobility matrix. This is done here by using the RFD method presented in Sec. V C, in Eqs. (21) and (22). The values of $\boldsymbol{M}(h,\theta)$ in the dummy position and orientation required by the RFD method are obtained by interpolating the mobility matrix data computed through hydrodynamic simulations and discussed in Sec. IV. Hence, all our results will refer to a spheroid with $AR = 8$.

A. Translational drift

We start our analysis by considering the z-component of the translational drift velocity, i.e., the component normal to the wall. Figure 14 shows $\left\langle \frac{\Delta r_z}{\Delta t} \right\rangle$ as a function of h and parametric in θ. For symmetry, only the range $\theta \in [0, \pi/2]$ is investigated. We report both the direct computation of the divergence terms in Eqs. (26) and (27) from the mobility data on the grid (triangles) and the approximation computed through the RFD in Eqs. (21) and (22) (circles). A quite good

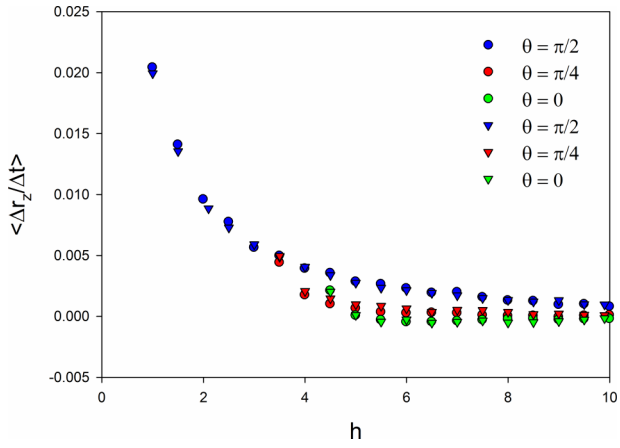

FIG. 14. Dimensionless drift velocity in direction z as a function of h, for different θ-values (colors). Circles represent the values computed through the RFD (Eqs. (21) and (22)) and triangles represent the values obtained by a direct computation of the "convective terms" (see text). A positive value means that the drift velocity z-component is directed away from the wall.

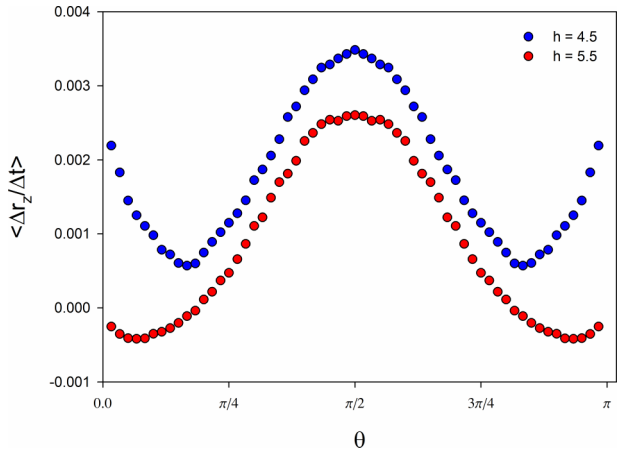

FIG. 15. Dimensionless drift velocity in direction z as a function of θ for two different particle wall-distances.

agreement is found between the two methods of computation. The drift velocity in Fig. 14 is a positive monotonically increasing function as h goes to zero in a range of θ between some critical value and $\pi/2$. For θ-values lower than such a critical angle (see, e.g., the case at $\theta = 0$), by decreasing the particle-wall distance, the drift velocity component initially decreases becoming negative, passes through a minimum, and then becomes positive again. This behavior differs from that of a sphere where a positive monotonically increasing drift as the sphere-wall distance reduces is always found.[39]

Figure 15 reports $\left\langle \frac{\Delta r_z}{\Delta t} \right\rangle$ as a function of θ for two values of h. The trends show a complex non-monotonic behavior of the z-component of drift velocity with respect to θ, with two minima and a maximum in the interval $\theta \in [0, \pi]$. In addition, the red symbols ($h = 5.5$) also show the existence of zero drift velocity angles, which are not present for a closer particle-wall distance.

In all the above results, the drift velocity has been calculated with complete Eq. (26). In Sec. IV, however, we showed that the components of $\boldsymbol{M}_b$ are one order of magnitude smaller than those of $\boldsymbol{M}_a$. It is then interesting to quantify the error committed by neglecting the term $k_B T \boldsymbol{\mathcal{R}} \cdot \boldsymbol{M}_b(h,\theta)$ when evaluating the left-hand side of Eq. (26). In Fig. 16, we report the total drift velocity (circles) and the sole contribution of the term $k_B T \boldsymbol{\nabla} \cdot \boldsymbol{M}_a(h,\theta)$ (squares). In other words, the circles in Fig. 16 are the same data already reported in Fig. 14. It clearly appears that neglecting the rotational divergence term, i.e., neglecting the matrix $\boldsymbol{M}_b$, induces a (relatively) large quantitative error and, more importantly, also changes the qualitative behavior of the drift velocity: notice, for instance, the absence of the negative minimum for the case $\theta = 0$.

It is well known in the literature that a sphere diffusing near a confining wall experiences a drift velocity only in the direction normal to the wall, driving the particle away from the wall.[39] In contrast, a spheroidal particle experiences a drift velocity in the x-direction as well. In Fig. 17, we report $\left\langle \frac{\Delta r_x}{\Delta t} \right\rangle$ as a function of θ for four different values of h. Three zeros of the "horizontal" drift velocity $\left\langle \frac{\Delta r_x}{\Delta t} \right\rangle$ are found, at $\theta = 0$, $\pi/2$ and π, for all the values of h. This component of the drift velocity also displays a minimum and a maximum, respectively, for $\theta \approx \pi/4$ and $3\pi/4$. While for an arbitrary value of (h,θ), the x-component of the drift velocity is not zero and is comparable in magnitude with the z-component, the symmetry of the trends in Fig. 17 implies that

$$\int_0^{\pi} \left\langle \frac{\Delta r_x(h,\theta)}{\Delta t} \right\rangle d\theta = 0. \tag{28}$$

As expected, there is no net drift velocity in directions different from z. Finally, the component $\left\langle \frac{\Delta r_y}{\Delta t} \right\rangle$ of the drift is found to be identically zero in the whole intervals of h and θ.

B. Rotational drift

We now turn to the analysis of the rotational drift velocity. In Fig. 18, we report the rotational drift around the z-direction, $\left\langle \frac{\Delta p_z}{\Delta t} \right\rangle$, as a function of θ for three different values of h. For $h = 4.5$, the trend shows a minimum and a maximum at $\theta = 0$ and $\theta = \pi$. In contrast, as the particle-wall distance h decreases, $\left\langle \frac{\Delta p_z}{\Delta t} \right\rangle$ becomes a linear function of θ in an enlarging range of θ. It is important to notice that, for $\theta < \pi/2$, the orientational drift velocity is negative, whereas for $\theta > \pi/2$, it is positive. This means that $\boldsymbol{p}$ always rotates so that its z-component tends to become zero, i.e., the leading edge of the spheroid is in any event attracted towards $\theta = \pi/2$.

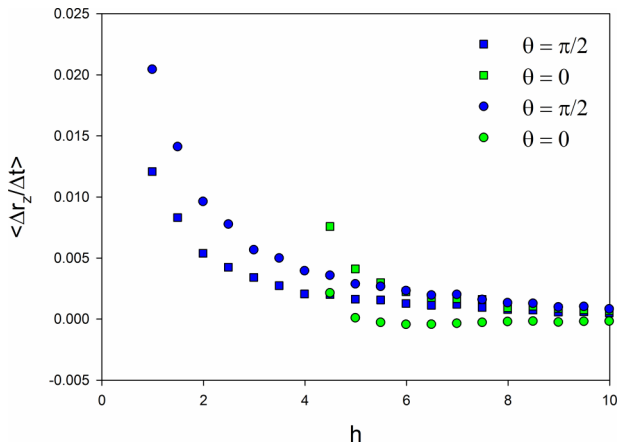

FIG. 16. Dimensionless drift velocity in direction z as a function of h, for two different θ-values. Square symbols represent the contribution of $k_B T \boldsymbol{\nabla} \cdot \boldsymbol{M}_a(h,\theta)$ only in Eq. (26), while circles are the total drift velocity along z.

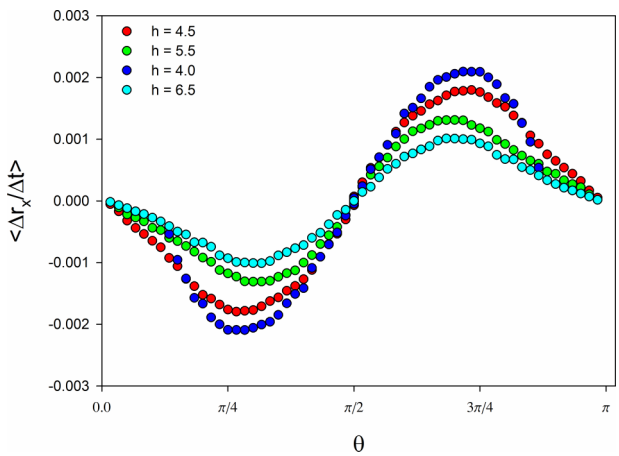

FIG. 17. Dimensionless drift velocity in direction x as a function of θ, for different h-values.

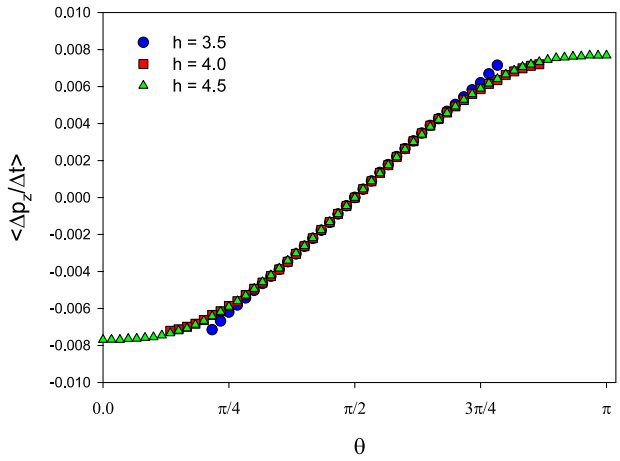

FIG. 18. Dimensionless orientational drift velocity in direction z as a function of θ, for different h-values. Because of the change of sign of the orientational drift velocity around $\theta = \pi/2$, the spheroid tends to stay parallel to the wall (see text).

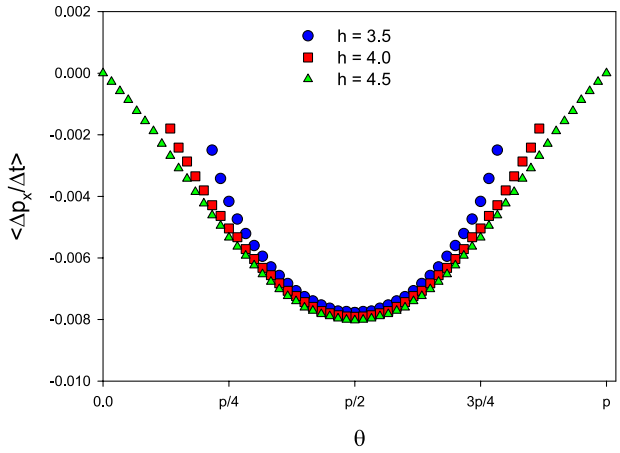

FIG. 19. Dimensionless orientational drift velocity in direction x as a function of θ, for different h-values.

In Fig. 19, we plot $\left\langle \frac{\Delta p_x}{\Delta t} \right\rangle$ as a function of θ for three different h-values. The x-component of the orientational drift velocity is negative in the whole interval $\theta \in [0, \pi]$. Similarly to what occurs for the z-component of the rotational drift velocity, there is no change in the qualitative behavior of $\left\langle \frac{\Delta p_x}{\Delta t} \right\rangle$ as the particle-wall distance is reduced. For all the h-values investigated, a minimum in $\theta = \frac{\pi}{2}$ shows. Notice that, for whatever h, by taking the average of $\left\langle \frac{\Delta p_x(h,\theta)}{\Delta t} \right\rangle$ over the whole unit sphere, there is no net orientational drift velocity in the x-direction.

Finally, similarly to what happens for the y-component of the translational drift velocity analyzed in Sec. VI B, it can be shown that $\left\langle \frac{\Delta p_y}{\Delta t} \right\rangle$ is identically zero in the whole interval (h, θ).

VII. CONCLUSIONS

In this paper, we have studied the hydrodynamics and the Brownian motions of a spheroid suspended in a quiescent Newtonian fluid near a rigid wall. We have carried out Finite Element Method (FEM) simulations to characterize the hydrodynamic interactions of a spheroid with an infinite plane wall. In particular, we have computed the mobility matrix in the range of positions and orientations covering all possible particle-wall configurations. We have found that the translational mobility is significantly reduced as the spheroid-wall distance decreases, especially when the particle is oriented parallel to the wall; on the other hand, the rotational mobility is reduced only when the particle-wall distance is very small, less than the spheroid major semi-axis length. The presence of the wall also induces a rotational-translational coupling with a complex dependence on both the particle-wall distance and orientation.

We also studied the Brownian motion of a spheroidal particle in the presence of a wall, by formulating a discretized version of the appropriate Langevin equation. The presence of particle-wall hydrodynamic interactions leads to additional convective terms in the Langevin equation, which are required to recover the correct equilibrium distribution. These convective terms depend on the spatial and orientational divergences of the mobility matrix and induce translational and rotational drift velocities. Unlike the case of spherical particles, the translational drift velocity is not a strictly positive monotonic increasing function as the spheroid approaches the wall and, for some configurations, it can also become negative, pointing towards the wall. The orientational drift velocities depend on the orientation angle but remain essentially unchanged as the spheroid approaches the wall. The net effect (if small) of the orientational drift is to align the spheroid parallel to the wall. The results presented in this paper illustrate that the hydrodynamics and the Brownian motions of a spheroid near a rigid wall significantly differ from those of a sphere-wall system.

In concluding, we would like to emphasize that the Langevin equation presented in this paper (Secs. V A and V B), together with the numerical recipes for calculating the "convective terms" (Sec. V C), is in no way limited to the situation tackled here, i.e., for a spheroid in the presence of a single plane wall, but is completely general, for an axisymmetric Brownian particle. The effects of a second infinite parallel wall and of other non-uniaxial confinements (e.g., near to corners), which may be of interest in microfluidics applications, can then (and hopefully will) be investigated, by the same equations, in future work.

ACKNOWLEDGMENTS

We would like to thank the anonymous referees for their suggestions that led to a significant improvement of our work. Specifically, we are particularly grateful to one of the referees, who signaled a mistake in the original version of the manuscript and in the corresponding numerical results, which has now been corrected.

APPENDIX A: EVALUATION OF ORIENTATIONAL DIVERGENCE TERMS IN THE LANGEVIN EQUATION THROUGH RANDOM FINITE DIFFERENCE APPROXIMATION

In this Appendix, we give the proof of Eq. (22). Let us consider an arbitrary small number ϵ. It is possible to express the matrix $\boldsymbol{A}(\boldsymbol{r}, \boldsymbol{p} + \epsilon \Delta \boldsymbol{q} \times \boldsymbol{p})$ as a Taylor series around the vector $\boldsymbol{p} = \boldsymbol{p}_0$. The correct gradient operator on the unit sphere for a Taylor expansion has been shown to be[45]

$$\nabla_p = \boldsymbol{p} \times \frac{\partial}{\partial \boldsymbol{p}} \times \boldsymbol{p} \tag{A1}$$

that can be alternatively expressed as

$$\nabla_p = \frac{\partial}{\partial \boldsymbol{p}} - \boldsymbol{p}(\boldsymbol{p} \cdot \frac{\partial}{\partial \boldsymbol{p}}). \tag{A2}$$

The second term is required to ensure that the gradient is tangent to the unit sphere. By writing the tensor $\boldsymbol{A}(\boldsymbol{r}, \boldsymbol{p} + \epsilon \Delta \boldsymbol{q} \times \boldsymbol{p})$ as a Taylor expansion around a generic orientation vector $\boldsymbol{p} = \boldsymbol{p}_0$, we get

$$\boldsymbol{A}(\boldsymbol{r}, \boldsymbol{p}_0 + \epsilon \Delta \boldsymbol{q} \times \boldsymbol{p}_0) = \boldsymbol{A}(\boldsymbol{r}, \boldsymbol{p}_0) + \epsilon [(\nabla_p \cdot (\Delta \boldsymbol{q} \times \boldsymbol{p})) \boldsymbol{A}(\boldsymbol{r}, \boldsymbol{p})]|_{\boldsymbol{p}=\boldsymbol{p}_0} + O(\epsilon^2). \tag{A3}$$

Substituting this expression in the right-hand side of Eq. (22), we obtain

$$\lim_{\epsilon \to 0} \frac{1}{\epsilon} \left\langle (\boldsymbol{A}(\boldsymbol{r}, \boldsymbol{p}_0 + \epsilon \Delta \boldsymbol{q} \times \boldsymbol{p}_0) \cdot \Delta \boldsymbol{q} - \boldsymbol{A}(\boldsymbol{r}, \boldsymbol{p}_0) \cdot \Delta \boldsymbol{q}) \right\rangle = \left\langle [(\nabla_p \cdot (\Delta \boldsymbol{q} \times \boldsymbol{p})) \boldsymbol{A}(\boldsymbol{r}, \boldsymbol{p})]|_{\boldsymbol{p}=\boldsymbol{p}_0} \cdot \Delta \boldsymbol{q} \right\rangle + O(\epsilon^2). \tag{A4}$$

Now we can rewrite the right-hand side by components adopting Einstein notation and neglecting the $O(\epsilon^2)$ terms,

$$\left\langle [(\nabla_p \cdot (\Delta \boldsymbol{q} \times \boldsymbol{p})) \boldsymbol{A}(\boldsymbol{r}, \boldsymbol{p})]|_{\boldsymbol{p}=\boldsymbol{p}_0} \cdot \Delta \boldsymbol{q} \right\rangle = \left\langle \left\{ \left[\frac{\partial}{\partial p_i} - p_i \left(p_n \frac{\partial}{\partial p_n} \right) \right] \varepsilon_{ijk} \Delta q_j p_k \left(A_{lm}(\boldsymbol{r}, \boldsymbol{p}) \right) \right\} \Big|_{\boldsymbol{p}=\boldsymbol{p}_0} \Delta q_m \boldsymbol{e}_l \right\rangle. \tag{A5}$$

In this equation, ε_{ijk} is the Levi-Civita symbol and the derivatives with respect to p_i and p_n are applied to $A_{lm}(\boldsymbol{r}, \boldsymbol{p})$ only; the whole expression is evaluated at $\boldsymbol{p} = \boldsymbol{p}_0$. From the definition of the moments of $\Delta \boldsymbol{q}$ reported in Eqs. (23), it follows that

$$\left\langle \Delta q_j \Delta q_m \right\rangle = \delta_{jm}. \tag{A6}$$

Thus, the right-hand side of Eq. (A4) becomes

$$\frac{\partial}{\partial p_i} \left[\{ \varepsilon_{ijk} p_k \left(A_{lj}(\boldsymbol{r}, \boldsymbol{p}) \right) \} |_{\boldsymbol{p}=\boldsymbol{p}_0} \right] \boldsymbol{e}_l - p_i \left(p_n \frac{\partial}{\partial p_n} \right) \left[\{ \varepsilon_{ijk} p_k \left(A_{lj}(\boldsymbol{r}, \boldsymbol{p}) \right) \} |_{\boldsymbol{p}=\boldsymbol{p}_0} \right] \boldsymbol{e}_l. \tag{A7}$$

By permutating the indices in the Levi-Civita operator, the first term becomes

$$\frac{\partial}{\partial p_i} \left[\{ \varepsilon_{jki} p_k \left(A_{lj}(\boldsymbol{r}, \boldsymbol{p}) \right) \} |_{\boldsymbol{p}=\boldsymbol{p}_0} \right] \boldsymbol{e}_l = \left[\left(\boldsymbol{p} \times \frac{\partial}{\partial \boldsymbol{p}} \right) \cdot \boldsymbol{A}(\boldsymbol{r}, \boldsymbol{p}) \right] \Big|_{\boldsymbol{p}=\boldsymbol{p}_0} = \mathcal{R} \cdot \boldsymbol{A}(\boldsymbol{r}, \boldsymbol{p})|_{\boldsymbol{p}=\boldsymbol{p}_0}. \tag{A8}$$

The second term vanishes identically because $\varepsilon_{jki} p_k p_i = 0$.

In conclusion, we obtain

$$\lim_{\epsilon \to 0} \frac{1}{\epsilon} \left\langle (\boldsymbol{A}(\boldsymbol{r}, \boldsymbol{p}_0 + \epsilon \Delta \boldsymbol{q} \times \boldsymbol{p}_0) \cdot \Delta \boldsymbol{q} - \boldsymbol{A}(\boldsymbol{r}, \boldsymbol{p}_0) \cdot \Delta \boldsymbol{q}) \right\rangle = \mathcal{R} \cdot \boldsymbol{A}(\boldsymbol{r}, \boldsymbol{p})|_{\boldsymbol{p}=\boldsymbol{p}_0}. \tag{A9}$$

Since this procedure is valid for any arbitrary vector $\boldsymbol{p}_0$, Eq. (A9) holds for all vectors $\boldsymbol{p}$.

APPENDIX B: ON THE *p*-NORM PRESERVING TERM IN THE LANGEVIN EQUATION

In this Appendix, we explicitly compute the average of the term $\frac{1}{2} \Delta \boldsymbol{\Theta}_B(t) \cdot [\boldsymbol{p}(t) \Delta \boldsymbol{\Theta}_B(t) - \Delta \boldsymbol{\Theta}_B(t) \boldsymbol{p}(t)]$ appearing in Eq. (14). In addition, we show that the above term recovers the orientational drift discussed by Cobb and Butler[25] when considering the diffusion of an unconfined thin rod.

We start by considering the definition of $\Delta \boldsymbol{\Theta}_B(t)$; according to Eq. (18) we have

$$\Delta \boldsymbol{\Theta}_B(t) = \sqrt{2 k_B T \Delta t} \left[\boldsymbol{m}_{\mathrm{x}}^T \cdot \Delta \boldsymbol{N}_1 + \boldsymbol{m}_2 \cdot \Delta \boldsymbol{N}_2 \right], \tag{B1}$$

where we define the matrices $\boldsymbol{m}_{\mathrm{x}}^T$ and $\boldsymbol{m}_2$ as follows:

$$\boldsymbol{m} = \begin{bmatrix} \boldsymbol{m}_1 & \boldsymbol{m}_{\mathrm{x}} \\ \boldsymbol{m}_{\mathrm{x}}^T & \boldsymbol{m}_2 \end{bmatrix}, \tag{B2}$$

that is, to say, as submatrices of the matrix $\boldsymbol{m}$. Notice that, for clarity, we dropped the dependencies of $\boldsymbol{m}$ on $\boldsymbol{r}(t)$ and $\boldsymbol{p}(t)$. By substituting Eq. (B1) in $\left\langle \frac{1}{2} \Delta \boldsymbol{\Theta}_B(t) \cdot (\boldsymbol{p}(t) \Delta \boldsymbol{\Theta}_B(t) - \Delta \boldsymbol{\Theta}_B(t) \boldsymbol{p}(t)) \right\rangle$, we obtain

$$k_B T \Delta t \, \boldsymbol{p} \cdot \left\langle (\boldsymbol{m}_{\mathrm{x}}^T \cdot \Delta \boldsymbol{N}_1 + \boldsymbol{m}_2 \cdot \Delta \boldsymbol{N}_2)(\boldsymbol{m}_{\mathrm{x}}^T \cdot \Delta \boldsymbol{N}_1 + \boldsymbol{m}_2 \cdot \Delta \boldsymbol{N}_2) \right\rangle - k_B T \Delta t \, \boldsymbol{p} \left\langle (\boldsymbol{m}_{\mathrm{x}}^T \cdot \Delta \boldsymbol{N}_1 + \boldsymbol{m}_2 \cdot \Delta \boldsymbol{N}_2)^2 \right\rangle. \tag{B3}$$

Rewriting the above expression in indicial notation

$$\begin{aligned} &+ k_B T \Delta t \, p_i \left\langle (m_{\mathrm{x},ij}^T \Delta N_{1,j} + m_{2,ij} \Delta N_{2,j})(m_{\mathrm{x},kl}^T \Delta N_{1,l} + m_{2,kl} \Delta N_{2,l}) \right\rangle \boldsymbol{e}_k \\ &- k_B T \Delta t \, p_k \left\langle (m_{\mathrm{x},ij}^T \Delta N_{1,j} m_{\mathrm{x},il}^T \Delta N_{1,l} + m_{\mathrm{x},ij}^T \Delta N_{1,j} m_{2,il}^T \Delta N_{2,l} + m_{2,ij} \Delta N_{2,j} m_{2,il} \Delta N_{2,l}) \right\rangle \boldsymbol{e}_k \end{aligned} \tag{B4}$$

(with $\boldsymbol{e}_k$ the unit vectors of the fixed frame), we now use average properties (20) of $\boldsymbol{N}_1$ and $\boldsymbol{N}_2$ to obtain

$$k_B T \Delta t\, p_i (m^T_{\mathrm{x},ij} m^T_{\mathrm{x},kj} + m_{2,ij} m_{2,kj}) \boldsymbol{e}_k - k_B T \Delta t\, p_k (m^T_{\mathrm{x},ij} m^T_{\mathrm{x},ij} + m_{2,ij} m_{2,ij}) \boldsymbol{e}_k \tag{B5}$$

or, in tensor notation,

$$\left\langle \frac{1}{2} \Delta \boldsymbol{\Theta}_B(t) \cdot (\boldsymbol{p}(t) \Delta \boldsymbol{\Theta}_B(t) - \Delta \boldsymbol{\Theta}_B(t) \boldsymbol{p}(t)) \right\rangle = k_B T \Delta t\, \boldsymbol{p} \cdot (\boldsymbol{m}^T_{\mathrm{x}} \cdot \boldsymbol{m}_{\mathrm{x}} + \boldsymbol{m}_2 \cdot \boldsymbol{m}_2) - k_B T \Delta t\, \boldsymbol{p} (\boldsymbol{m}^T_{\mathrm{x}} : \boldsymbol{m}_{\mathrm{x}} + \boldsymbol{m}_2 : \boldsymbol{m}_2). \tag{B6}$$

If we now consider the diffusion of an unconfined thin rod, it is $\boldsymbol{m}_{\mathrm{x}} = 0$, because there is no roto-translational coupling, while $\boldsymbol{m}_2 = \sqrt{M_r} \boldsymbol{I}$, where M_r is the rotational mobility of the rod perpendicular to its major axis. Inserting these expressions into Eq. (B6), we obtain

$$\left\langle \frac{1}{2} \Delta \boldsymbol{\Theta}_B(t) \cdot (\boldsymbol{p}(t) \Delta \boldsymbol{\Theta}_B(t) - \Delta \boldsymbol{\Theta}_B(t) \boldsymbol{p}(t)) \right\rangle = k_B T M_r \Delta t\, \boldsymbol{p} \cdot \boldsymbol{I} - k_B T\, M_r \Delta t\, \boldsymbol{p} Tr(\boldsymbol{I}) = -2 k_B T\, M_r \Delta t\, \boldsymbol{p}, \tag{B7}$$

which is the result obtained by Cobb and Butler[25] for an unconfined rod.

[1] T. M. Squires and S. R. Quake, "Microfluidics: Fluid physics at the nanoliter scale," Rev. Mod. Phys. **77**, 977 (2005).
[2] R. A. Petros and J. M. DeSimone, "Strategies in the design of nanoparticles for therapeutic applications," Nat. Rev. Drug Discovery **9**, 615–627 (2010).
[3] E. Lauga, M. Brenner, and H. Stone, "Microfluidics: The no-slip boundary condition," in *Handbook of Experimental Fluid Mechanics* (Springer, Berlin/Heidelberg, 2007), pp. 1219–1240.
[4] J. Happel and H. Brenner, in *Low Reynolds Number Hydrodynamics: With Special Applications to Particulate Media* (Springer, 1983), Vol. 1.
[5] S. Kim and S. Seppo, *Microhydrodynamics* (Dover Publications, 2005).
[6] P. Holmqvist, J. K. Dhont, and P. R. Lang, "Anisotropy of Brownian motion caused only by hydrodynamic interaction with a wall," Phys. Rev. E **74**, 021402 (2006).
[7] M. D. Carbajal-Tinoco, R. Lopez-Fernandez, and J. L. Arauz-Lara, "Asymmetry in colloidal diffusion near a rigid wall," Phys. Rev. Lett. **99**, 138303 (2007).
[8] M. A. Bevan and D. C. Prieve, "Hindered diffusion of colloidal particles very near to a wall: Revisited," J. Chem. Phys. **113**, 1228–1236 (2000).
[9] P. Holmqvist, J. K. G. Dhont, and P. R. Lang, "Colloidal dynamics near a wall studied by evanescent wave light scattering: Experimental and theoretical improvements and methodological limitations," J. Chem. Phys. **126**, 044707 (2007).
[10] L. P. Faucheux and A. J. Libchaber, "Confined Brownian motion," Phys. Rev. E **49**, 5158 (1994).
[11] B. Lin, J. Yu, and S. A. Rice, "Direct measurements of constrained Brownian motion of an isolated sphere between two walls," Phys. Rev. E **62**, 3909 (2000).
[12] E. R. Dufresne, D. Altman, and D. G. Grier, "Brownian dynamics of a sphere between parallel walls," Europhys. Lett. **53**, 264 (2001).
[13] H. Eral, J. Oh, D. Van Den Ende, F. Mugele, and M. Duits, "Anisotropic and hindered diffusion of colloidal particles in a closed cylinder," Langmuir **26**, 16722–16729 (2010).
[14] J. Dhont, *An Introduction to Dynamics of Colloids* (Elsevier, 1996).
[15] Y. Han, A. Alsayed, M. Nobili, J. Zhang, T. C. Lubensky, and A. G. Yodh, "Brownian motion of an ellipsoid," Science **314**, 626–630 (2006).
[16] Y. Han, A. Alsayed, M. Nobili, and A. G. Yodh, "Quasi-two-dimensional diffusion of single ellipsoids: Aspect ratio and confinement effects," Phys. Rev. E **80**, 011403 (2009).
[17] G. Li and J. X. Tang, "Diffusion of actin filaments within a thin layer between two walls," Phys. Rev. E **69**, 061921 (2004).
[18] R. Duggal and M. Pasquali, "Dynamics of individual single-walled carbon nanotubes in water by real-time visualization," Phys. Rev. Lett. **96**, 246104 (2006).
[19] R. Colin, M. Yan, L. Chevry, J.-F. Berret, and B. Abou, "3d rotational diffusion of micrometric wires using 2d video microscopy," Europhys. Lett. **97**, 30008 (2012).
[20] D. Mukhija and M. J. Solomon, "Translational and rotational dynamics of colloidal rods by direct visualization with confocal microscopy," J. Colloid Interface Sci. **314**, 98–106 (2007).
[21] F. C. Cheong and D. G. Grier, "Rotational and translational diffusion of copper oxide nanorods measured with holographic video microscopy," Opt. Express **18**, 6555–6562 (2010).
[22] S. Ota, T. Li, Y. Li, Z. Ye, A. Labno, X. Yin, M.-R. Alam, and X. Zhang, "Brownian motion of tethered nanowires," Phys. Rev. E **89**, 053010 (2014).
[23] H. Lowen, "Brownian dynamics of hard spherocylinders," Phys. Rev. E **50**, 1232 (1994).
[24] Y.-G. Tao, W. Den Otter, J. Padding, J. Dhont, and W. Briels, "Brownian dynamics simulations of the self-and collective rotational diffusion coefficients of rigid long thin rods," J. Chem. Phys. **122**, 244903 (2005).
[25] P. D. Cobb and J. E. Butler, "Simulations of concentrated suspensions of rigid fibers: Relationship between short-time diffusivities and the long-time rotational diffusion," J. Chem. Phys. **123**, 054908 (2005).
[26] Y.-G. Tao, W. Den Otter, J. Dhont, and W. Briels, "Isotropic-nematic spinodals of rigid long thin rodlike colloids by event-driven Brownian dynamics simulations," J. Chem. Phys. **124**, 134906 (2006).
[27] S. N. Naess and A. Elgsaeter, "Singularity-free Brownian dynamics analyses of rotational dynamics: Non-spherical nanoparticles in solution," Macromol. Theory Simul. **14**, 300–304 (2005).
[28] M. Makino and M. Doi, "Brownian motion of a particle of general shape in Newtonian fluid," J. Phys. Soc. Jpn. **73**, 2739–2745 (2004).
[29] M. Doi and M. Makino, "Motion of micro-particles of complex shape," Prog. Polym. Sci. **30**, 876–884 (2005).
[30] I. M. Ilie, W. K. den Otter, and W. J. Briels, "Rotational Brownian dynamics simulations of clathrin cage formation," J. Chem. Phys. **141**, 065101 (2014).
[31] M. Doi and S. Edwards, *The Theory of Polymer Dynamics* (Claredon, Oxford, 1986).
[32] J. W. Swan and J. F. Brady, "Particle motion between parallel walls: Hydrodynamics and simulation," Phys. Fluids **22**, 103301 (2010).
[33] J. Padding and W. Briels, "Translational and rotational friction on a colloidal rod near a wall," J. Chem. Phys. **132**, 054511 (2010).
[34] A. Malevanets and R. Kapral, "Mesoscopic model for solvent dynamics," J. Chem. Phys. **110**, 8605–8613 (1999).
[35] R. Hsu and P. Ganatos, "The motion of a rigid body in viscous fluid bounded by a plane wall," J. Fluid Mech. **207**, 29–72 (1989).
[36] H. Keh and C. Tseng, "Slow motion of an arbitrary axisymmetric body along its axis of revolution and normal to a plane surface," Int. J. Multiphase Flow **20**, 185–210 (1994).
[37] P. E. Kloeden and E. Platen, in *Numerical Solution of Stochastic Differential Equations* (Springer, 1992), Vol. 23.
[38] H. C. Öttinger, *Stochastic Processes in Polymeric Fluids: Tools and Examples for Developing Simulation Algorithms* (Springer Verlag, 1996).
[39] A. Lau and T. C. Lubensky, "State-dependent diffusion: Thermodynamic consistency and its path integral formulation," Phys. Rev. E **76**, 011123 (2007).
[40] M. Hutter and H. Ottinger, "Fluctuation-dissipation theorem, kinetic stochastic integral and efficient simulations," J. Chem. Soc., Faraday Trans. **94**, 1403–1405 (1998).
[41] S. Delong, F. B. Usabiaga, R. Delgado-Buscalioni, B. E. Griffith, and A. Donev, "Brownian dynamics without Green's functions," J. Chem. Phys. **140**, 134110 (2014).
[42] P. Lançon, G. Batrouni, L. Lobry, and N. Ostrowsky, "Drift without flux: Brownian walker with a space-dependent diffusion coefficient," Europhys. Lett. **54**, 28 (2001).
[43] G. Volpe, L. Helden, T. Brettschneider, J. Wehr, and C. Bechinger, "Influence of noise on force measurements," Phys. Rev. Lett. **104**, 170602 (2010).
[44] T. Brettschneider, G. Volpe, L. Helden, J. Wehr, and C. Bechinger, "Force measurement in the presence of Brownian noise: Equilibrium-distribution method versus drift method," Phys. Rev. E **83**, 041113 (2011).
[45] G. Marrucci and F. Greco, "Flow behavior of liquid crystalline polymers," Adv. Chem. Phys. **86**, 331–404 (1993).